Supporting Information for

DNA tensiometer reveals catch-bond detachment kinetics of kinesin-1, -2 and -3

Crystal R. Noell[1], Tzu-Chen Ma[1], Rui Jiang[1], Scott Mckinley[2], William O. Hancock*[1,3]

* Corresponding author.
Email: woh1@psu.edu

Supplementary Methods

Biotinylated MT

Tubulin was purified from bovine brain as previously described (Cleary et al., 2022; Uppalapati M, 2009), with the following modifications. After the 45 minute growth phase a 12-fold excess of EZ-link NHS-biotin (Thermo Fisher 20217) was added and incubation at 37℃ continued for another 30 minutes. Microtubules were then depolymerized, polymerized, and pelleted twice to obtain pure biotinylated tubulin. Tubulin concentration was measured by absorbance, and the fraction biotinylated measured using the Biocytin Kit (Thermo Fisher 28022).

Motor Expression, Purification and Oligo Conjugation

Drosophila melanogaster Kinesin-1-EGFP-SNAP-His_6 (aa 1-406) was expressed in Tuner (DE3) E.coli (Addgene #129764). Cells were grown in Terrific Broth (Sigma Aldrich) at 37℃ with shaking at 180 rpm for 4-6 hours until an OD of greater than 1 was reached, then induced with 120 mg IPTG and shaken overnight at 21℃. Cells were harvested the next day, pelleted, resuspended with 1x PBS, frozen, and stored at -80℃. *Rattus norvegicus* Kif1A (aa 1-351)-Kif1A neck linker (NL) (17aa)-Kinesin1 coiled-coil (aa 345-406)-EGFP-SNAP was expressed in Tuner (DE3) E.coli similarly to kinesin-1 (Addgene #229851). *Mus musculus* Kif3A (aa 1-342)-Kif3A NL (17aa)-Kinesin1 coiled-coil (aa 345-406)-EGFP-SNAP was expressed in BL21(DE3) E.coli (Addgene # 229852). Kif1A and Kif3A constructs were synthesized into the kinesin-1 construct backbone by GenScript. His_6 tagged GBP-SNAP in pet28a was also expressed and purified similarly (Feng et al., 2020; Feng et al., 2018; Gicking et al., 2022; Kubala et al., 2010).

Bacterial cell pellets (from 800 mL culture) were thawed and motors were purified via Ni affinity chromatography as described previously (Gicking et al., 2022; Gicking et al., 2019; Zaniewski et al., 2020). Motor proteins were eluted in a buffer containing 20 mM phosphate buffer, 500 mM sodium chloride, 500 mM imidazole, 10 μM ATP and 5 mM DTT. The concentration of pre-labeled motors was then measured by absorbance at 488 nm (using the EGFP extinction coefficient 55,900 $M^{-1}cm^{-1}$), and proteins were visualized with SDS PAGE.

Amine-terminated oligonucleotides (IDT) were resuspended and desalted into 200 mM sodium borate buffer, and the concentration measured by absorbance. The desalted oligo was then mixed with 20-fold excess of BG-GLA-NHS (NEB S9151S, dissolved in DMSO) in 100 mM sodium borate and 50% DMSO and incubated at RT for 30 min. The mixture was then desalted into 1x PBS buffer (containing 1 mM DTT and 1 mM $MgCl_2$). The elution profile was measured by absorbance and the fractions of BG-oligo were pooled. The pre- and post- labeled oligos were visualized on a 10% TBE-Urea gel and stained with SYBR green I. Excess BG-oligo was stored at -20℃.

Immediately following Ni column purification of motors, BG-oligo was mixed with the eluted motor at a 5:1 ratio and incubated on ice for 1 hr. The mixture was then diluted with 1x PBS + 1 mM $MgCl_2$ sufficient to reduce the imidazole concentration to below 80 mM, and a second Ni-affinity purification was carried out to remove the excess BG-oligo. The protein was eluted in the same elution buffer and flash frozen in liquid N_2 in the presence of 10 μM MgATP, 1 mM DTT and 10% sucrose. Final protein

concentration was measured by EGFP absorbance. SDS-PAGE and native PAGE were used to estimate the percentage of motors that have an oligo conjugated to them, typically ~50% were labeled. Oligo-labeled motors were kept at -80℃ for up to a year.

QDot Labeling

For labelling GFP motors, Qdots were functionalized with GFP-binding protein (GBP) as follows. QDot® ITKTM Amino (PEG) quantum dots (Thermo Fisher Q21541MP) were buffer exchanged by transferring 250uL into a 100K ultrafiltration unit and adding 1x PBS pH 7.4 to make up the filter volume of 4 mL. The sample was centrifuged to the original volume of 250 μL before more buffer was added and the process was repeated 3x. The Qdots were then transferred to a glass vial, BG-GLA-NHS was added in 50-fold excess in a 100 mM sodium borate buffer containing 50% DMSO (v/v), and the reaction incubated for 1 hr at room temperature on a rotator. Excess BG-GLA-NHS was removed by carrying out 5 complete buffer exchanges with a 100K centrifugal concentrating filter. The concentration of BG-Qdots was determined on a plate reader based on a calibration curve from the initial Qdot stock. BG-Qdots were then mixed with GBP-SNAP at a 1:50 ratio and incubated on ice for 1 hour. Qdot-GBP was stored at 4℃ for up to 6 months. On the day of an experiment, Qdot-GBP was mixed with GFP labeled motors at a 10:1 ratio to prevent multi-motor Qdots and incubated on ice for at least 15 minutes before visualization by TIRF.

Fitting Equations

Data in Figures 2, S5 and S6 were fit using MEMLET (Woody et al., 2016) to the following single exponential function:

$$\boldsymbol{y(t) = \frac{k e^{-kt}}{e^{-k t_{min}}}}$$

where *k* is the rate constant (inverse of the time constant) and t_{min} is the minimum cutoff of the distribution.

Data in Figure S4 were fit using MEMLET to the following bi-exponential function:

$$\boldsymbol{y(t) = \frac{\left(A k_1 e^{-k_1 t} + (1-A) k_2 e^{-k_2 t}\right)}{\left(A e^{-k_1 t_{min}}\right) + \left((1-A) e^{-k_2 t_{min}}\right)}}$$

Here A is the amplitude of the first phase, k_1 and k_2 are the rate constants (inverse time constants) of the two phases, and t_{min} is the minimum cutoff of the distribution. This approach corrects the amplitudes for missed events, which can differ for the two phases Cumulative distribution data in Figure 4 were fit by least squares in Matlab to the bi-exponential function:

$$\boldsymbol{y(t) = A_1\left(1 - e^{-\frac{(x-t_0)}{\tau_1}}\right) + (1-A_1)\left(1 - e^{-\frac{(x-t_0)}{\tau_2}}\right)}$$

Here $\boldsymbol{\tau_1}$ and $\boldsymbol{\tau_2}$ are time constants (inverse rate constants) of the two phases, A_1 is the amplitude of the first phase, and t_0 is the minimum cutoff time of the distribution. Amplitudes are normalized to account for missed short events as follows:

$$\boldsymbol{A_{1_{corrected}} = A_1 e^{\frac{t_0}{\tau_1}}}$$

$$\boldsymbol{A_{2_{corrected}} = (1 - A_1) e^{\frac{t_0}{\tau_2}}}$$

$$\boldsymbol{A_{1_{corrected_{relative}}} = \frac{A_{1_{corrected}}}{A_{1_{corrected}} + A_{2_{corrected}}}}$$

$$\boldsymbol{A_{2_{corrected_{relative}}} = \frac{A_{2_{corrected}}}{A_{1_{corrected}} + A_{2_{corrected}}}}$$

Inference strategy for the ramp duration parameter

The primary challenge in assessing ramp runs is that these segments can end for one of two reasons: either (1) the motor detaches, or (2) the motor reaches a distance sufficiently far from the anchor to enter a stalled state. By contrast, unloaded runs and stall segments all end in detachments from microtubules. So, while taking a simple average of segment durations will result in an "average time until detachment" for unloaded and stalled segments, this is not the case for ramps. Moreover, ambiguity as to when a ramp run begins further confirms that a simply average of ramp segment durations will lead to errors. This issue is similar to the one raised in Rayens et al. (Rayens et al., 2022) in which the authors sought to estimate the average stationary segment length for motor-lysosome complexes in vivo, even though the length of some stationary segments exceeded the length of the observation window.

One way to address the problem of truncated durations is to assume that state-switching satisfies the Markov property, which is to say that whether an agent switches states in a given time step is independent of states and switches that occurred during previous time steps. for continuous time Markov chains, models are expressed in terms of rates, and so the natural quantity of interest here is the detachment rate, which might commonly be denoted k_{off}. Within the text, we wish to compare ramp state properties to unloaded and stall states which are quantified in terms of their average duration. In this note we therefore write the detachment rate in terms of a duration parameter $\tau = 1/k_{\text{off}}$. Generically, the probability that a continuous-time Markov chain does not change state in a segment of time $[a, b]$ is given by the formula:

$$P(\text{No change during [a, b]}) = e^{-\int_a^b \kappa(t)dt},$$

where $\kappa(t)$ the (possibly evolving) rate at which changes occur. If we assume that the detachment rate $1/\tau$ is constant, then in any segment of length Δ, the probability that a motor does not detach is

$$P(\text{No change during [a, b]}) = e^{-\frac{\Delta}{\tau}},$$

Suppose that $(t_0, t_1, \ldots, t_n)$ are observation times of a tensiometer run and let T denote the time that a motor would detach were it not for transitions to stall. Then the probability that a detachment occurs in the interval $[t_k, t_{k+1})$ is product of the probabilities it does not detach in all preceding segments multiplied by the probability it does detach in the final one. This idea is shown in the diagram below. The initial green segments are ramps which may result in a detachment (yellow star), or

result in conversion to a stall state (red line) which always ends in a detachment. In describing our approach to inference, we denote the ramp durations $\{T_i\}_{i=1}^{N+M}$ and the stall durations are $\{S_i\}_{i=1}^{M}$. This notation scheme implies that there were *N* detachment events during ramp segments.

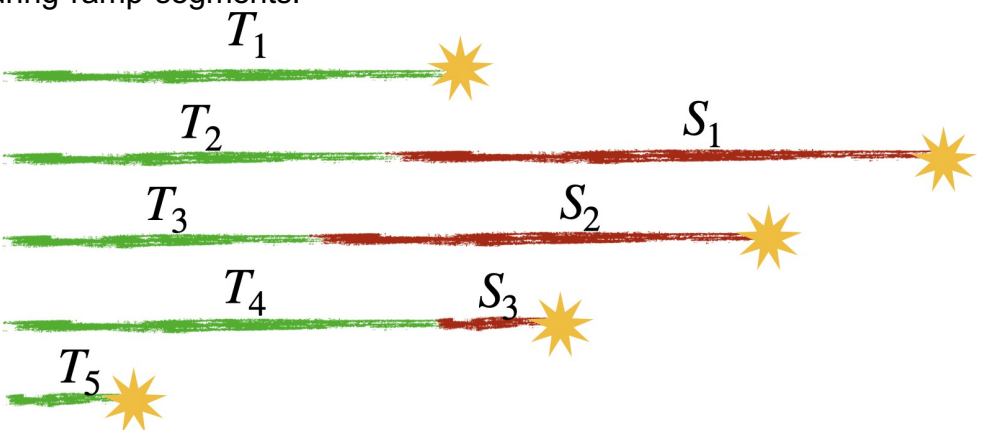

Mathematically, we write

$$P\big(T \in [t_k, t_{k+1})\big) = \Big(\prod_{i=1}^{k} e^{\frac{-(t_i - t_{i-1})}{\tau}}\Big)\left(1 - e^{\frac{-(t_{k+1} - t_k)}{\tau}}\right)$$
$$= e^{-\frac{-(t_k - t_0)}{\tau}}\left(1 - e^{\frac{-(t_{k+1} - t_k)}{\tau}}\right)$$

Assuming that time increments are evenly spaced and of size Δ, and also assuming that Δ is small compared to the duration parameter τ, we can take the first term of the Taylor expansion of the $(t_{k+1} - t_k)$ term and simplify:

Ramp with detachment: $P\big(T \in [t_k, t_{k+1})\big) \approx e^{\frac{-(t_k - t_0)}{\tau}}\frac{\Delta}{\tau}$

On the other hand, suppose that the motor switches to a stalled state after time t_k. Then the initial product of non-detaching segments remains the same, and final term is removed:

Ramp without detachment: $P\big(T \in [t_k, t_{k+1})\big) \approx e^{\frac{-(t_k - t_0)}{\tau}}$

To unify the notation, let 1_i^{det} denote the event that the *i* ramp run detached before reaching stall phase. We have

$$P\big(T \in [t_k, t_{k+1})\big) \approx \left(\frac{\Delta}{\tau}\right)^{1_i^{det}} e^{\frac{-(t_k - t_0)}{\tau}}$$

To perform inference on multiple runs, we assume they are independent and so, again, we can take a simple product. As described in the caption of Figure 1, let $\{T_i\}_{i=1}^{N+M}$ be an enumeration of ramp durations, where *N* is the number of ramps that detached and *M* is the number of ramps that reached a stall state. It follows that the likelihood of observing a set of trajectories *X* given a duration parameter τ can be written

$$P(X;\tau) = \prod_{i=1}^{N+M}\left(\frac{\Delta}{\tau}\right)^{1_i^{det}} e^{\frac{-T_i}{\tau}}$$
$$= \left(\frac{\Delta}{\tau}\right)^{N} e^{\frac{-\sum T_i}{\tau}}$$

From a Bayesian perspective, we can use this likelihood function to create a posterior distribution for the duration parameter τ. In this work we have used a scale-free uninformative prior (Robert, 1994) of the form $\pi(r) = r^{-1}$. Together with the likelihood, we have that the posterior distribution has the form

$$\pi(\tau|X) \overset{c}{=} P(X;\tau)\pi(\tau)$$
$$= \Delta^N \tau^{-(N+1)} e^{\frac{-\sum T_i}{\tau}}$$

where $\overset{c}{=}$ means "equals up to a constant depending only on X". Looking at the factors that depend only on τ this is an Inverse Gamma distribution.
In this way, we reach the conclusion that if T is the total time spent in the ramp states and if N is the number of detachments while in the ramp state, the posterior distribution for the duration parameter is

$$\pi(\tau|T,N) \sim \text{InvGamma}(N, T).$$

This means that it has pdf

$$f(t;N,T) = \frac{T^N}{\Gamma(N)} \frac{1}{t^{\alpha+1}} e^{\frac{-T}{\tau}}$$

and, most importantly for the purpose of estimation, the mean of the posterior distribution is simply T/N. In other words, the simple Bayes estimator for a collection of ramp segments is:

$$\hat{\tau} = \frac{T}{N} = \frac{\text{Total time in ramp phase}}{\text{Number of detachments in ramp phase}}$$

To set our $100(1-\alpha)$ %-credible regions, we used the middle-α probability range from the posterior distribution. This means that the 95% credible region is defined as the interval between the 0.025-quantile and 0.975-quantile of the posterior distribution. These regions are indicated as solid lines segments beneath the posterior distributions depicted in Figure 3 in the main text.

Compensating for difficulty in observing short runs

For unloaded and ramp runs there is a significant risk that short runs will be unobserved. For ramp runs, short ramp phases might be masked by the fluctuations that occur when the motor is detached. Meanwhile, short, unloaded runs might not be recognized among many motors in a wide field of view. Among kinesin-1 runs, for example, the shortest recorded unloaded run was 0.48s, despite the frame rate being significantly smaller. The minimum recorded times, t_{min} (seconds), for each category of run observations is as follows:

	Stall	Ramp	Unloaded
Kinesin-1	0.1	0.14	0.48
Kinesin-2	0.22	0.17	0.348
Kinesin-3	0.03	0.03	0.641

The likelihood function therefore needs to be adjusted to be conditioned on being greater than the minimum observation time for that cohort. Continuing with the notation from above (for convenience taking $t_0 = 0$, let T_i denote the ith run duration. Then the joint likelihood function is therefore

$$P(T \in [t_k, t_{k+1}) | T_i > t_{\min}) = \frac{P(T \in [t_k, t_{k+1}), T_i > t_{\min})}{P(T_i > t_{\min})}$$

$$\approx \frac{1_{t_k > t_{\min}} e^{\frac{-t_k}{\tau}} \Delta}{e^{\frac{-t_{\min}}{\tau}}}$$

$$= 1_{t_k > t_{\min}} e^{\frac{-(t_k - t_{\min})}{\tau}} \frac{\Delta}{\tau}$$

For a collection of paths χ, the likelihood function becomes

$$P(X | \tau, t_{\min}) = \prod_{i=1}^{N+M} 1_{T_i > t_{\min}} \left(\frac{\Delta}{\tau}\right)^{1_i^{det}} e^{\frac{-(T_i - t\_\min)}{\tau}}$$

$$= 1_{\min_i T_i > t_{\min}} \left(\frac{\Delta}{\tau}\right)^{N} e^{\frac{-(T_i - t\_\min)}{\tau}}$$

Note that for any fixed value τ, the maximum of the likelihood function over all $t_{\min}$ values is $t_{\min} = \min_i T_i$. Rather than constructing a joint Bayesian posterior for the pair (τ, $t_{\min}$), we simply adopted the maximum likelihood value for $t_{\min}$ within each cohort and proceeded as described above with the likelihood function

$$P(X; \tau) \left(\frac{\Delta}{\tau}\right)^{N} e^{\frac{-\sum_i (T_i - \min_j T_j)}{\tau}}$$

1

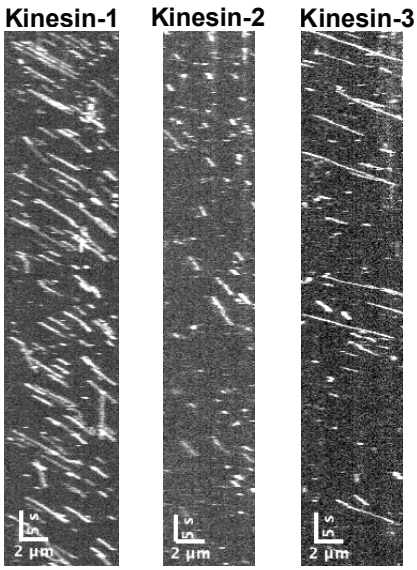

Figure. S1. Kymographs of unloaded GFP-labeled kinesins. GPF-labeled motors conjugated to their complimentary oligo were visualized via TIRF at a concentration of 1 nM at 5 fps. No neutravidin, Qdot or DNA are present in these unloaded controls. Of note, a portion of kinesin-3 unloaded run durations were limited by the length of the microtubules, meaning the unloaded duration is a lower limit.

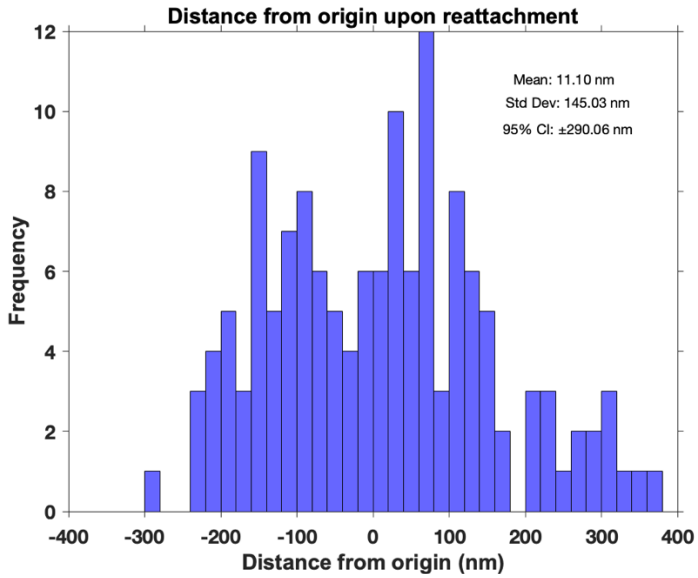

Figure. S2. Distribution of initial motor binding positions. The initial positions were measured for events where the motor was clearly dissociated from the microtubule and fluctuated around origin on its DNA tether (N=141). The zero position was determined as the center point around which the detached motor fluctuated. The initial motor binding position was determined by the first start point of a ramp. The width of the gaussian distribution, quantified by the SD, demonstrates the large search space of the motor attached to the flexible ~1-micron dsDNA tether. The mean of +11 nm likely results from some of the motors moving before the first frame acquisition, giving a small positive bias. The larger population seen at >+200 nm relative to <-200 nm may result from dissociation of motors that bind under assisting loads (negative displacements) and strengthening of motors that bind under hindering loads (positive displacements). Data are from kinesin-1 and kinesin-3 tensiometers.

Table S1. Fit results for unloaded, ramp, and stall durations

		Results from a Maximum Likelihood Estimator (MEMLET) (Fig. 2)		Results from Markov model coupled with Bayesian inference (Fig. 3)	
Motor	**State**	**τ (s)**	**95% CI (s)**	**τ (s)**	**95% CI (s)**
Kinesin-1	Unloaded	1.04	0.79 – 1.30	1.05	0.81 – 1.36
	Ramp			2.49	1.87 – 3.32
	Stall	3.01	2.30 – 3.79	3.05	2.43 – 3.83
Kinesin-2	Unloaded	1.07	0.85 – 1.35	1.09	0.88 – 1.34
	Ramp			0.97	0.87 – 1.08
	Stall	2.83	2.03 – 3.79	2.90	2.17 – 3.86
Kinesin-3	Unloaded	2.74	2.33 – 3.17	2.76	2.28 – 3.34
	Ramp			0.75	0.64 – 0.87
	Stall	1.89	1.53 – 2.31	1.90	1.60 – 2.25

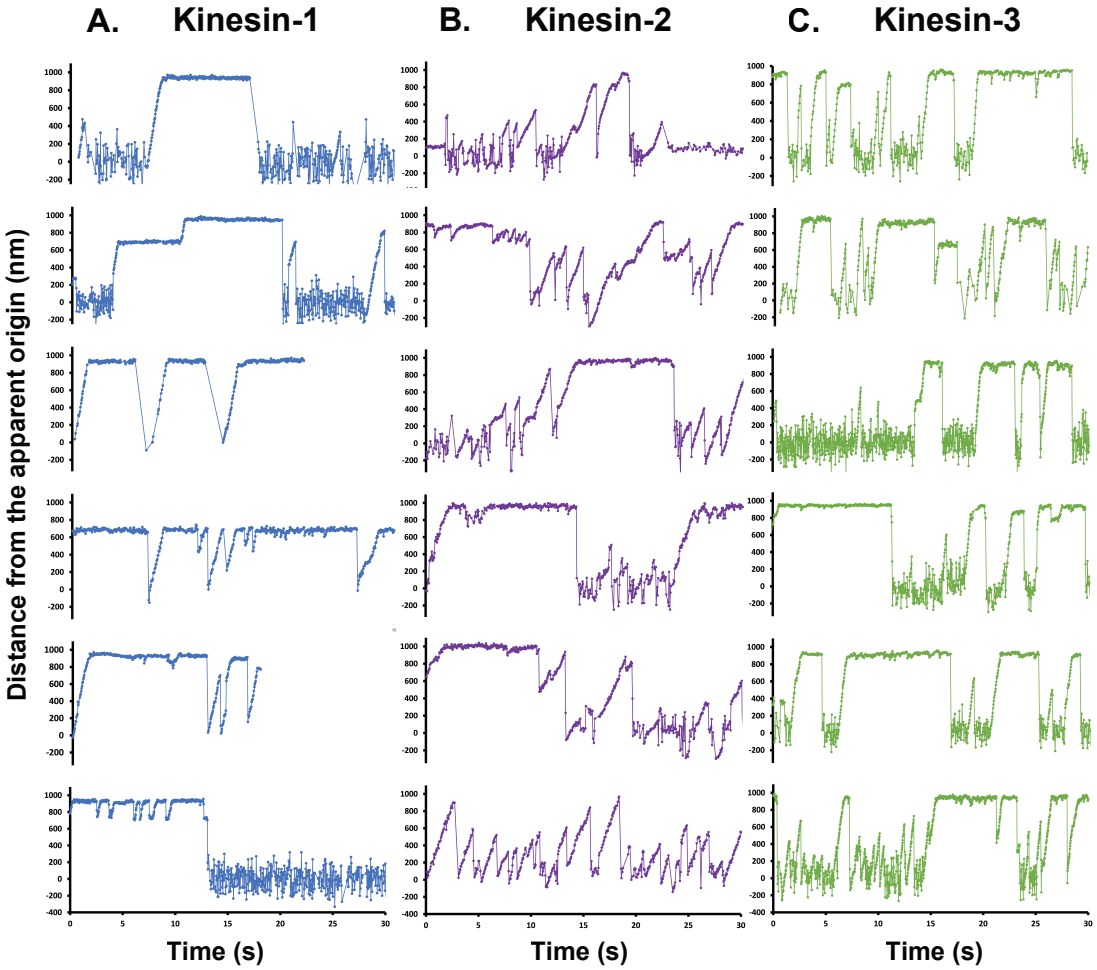

Figure. S3. Further kinesin tensiometer examples. Distance versus time plots of (A) kinesin-1, (B) kinesin-2 and (C) kinesin-3 traces. Notably, some stalls are very stable, whereas other (particularly for kinesin-2 and kinesin-3) show fluctuations, presumably due to small slips and backstepping at stall. Other features to note include pauses in the motile segments, small changes in velocity, and repeated ramps for kinesin-2. Roughly 20% of our tensiometers extended less than the expected 1 μm distance, stalling repeatedly at 500 nm or 800 nm. These apparently shorter DNA strands may result from DNA secondary structures or from primer binding at a secondary sequence. After in-depth comparison of the data we found that the stall durations, reattachment rates, and starting positions were unaffected by the shorter DNA length and thus included the shorter tensiometers in our data set.

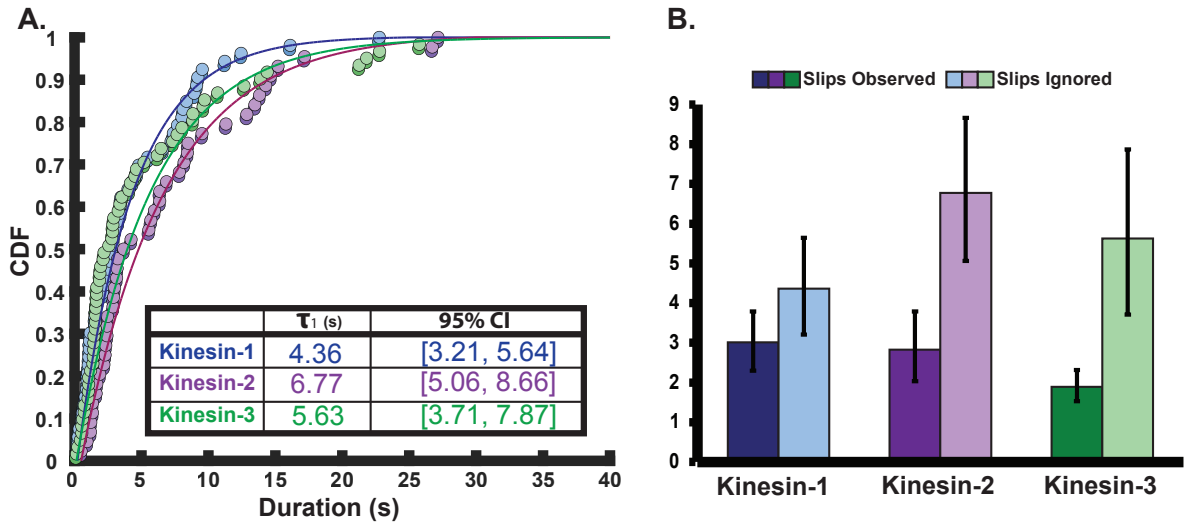

Figure. S4. Stall durations ignoring transient slip events at stall. In our stall duration analysis in Figure 2, we defined transient slip events, when the motor slips backward but not all the way to the origin, as terminating a stall plateau. However, functionally, such as in a tug-of-war with dynein, these slip events will only cause a transient displacement, and the motor will then rapidly reestablish a stall. Thus, they can be considered simply as fluctuations with the true end of a stall being when the motor returns to the origin, denoting full motor detachment. To quantify this functional stall duration, we ignored slip events and defined the end of stalls as the motor returning to the origin. (A) The CDF of these 'functional stall' durations was fit with a single exponential function using a maximum likelihood estimator (MEMLET). The resulting time constants are shown in the inset table. (B) A bar plot comparing time constants, where stalls are not ended by slips, and where they are. Time constants where stalls are not ended by slips were all longer than the values from Figure 2 (3.01 s, 2.83 s, and 1.89 s, respectively). The largest difference was seen for kinesin-2 and -3. The error bars are the 95% confidence intervals determined by MEMLET bootstrapping.

Table S2: Relative frequency of slips during stall plateaus.

	τ_{stall} no slips (s)	τ_{stall} with slips (s)	Ratio
Kinesin-1	3.01	4.36	1.5
Kinesin-2	2.83	6.77	2.4
Kinesin-3	1.89	5.63	3.0

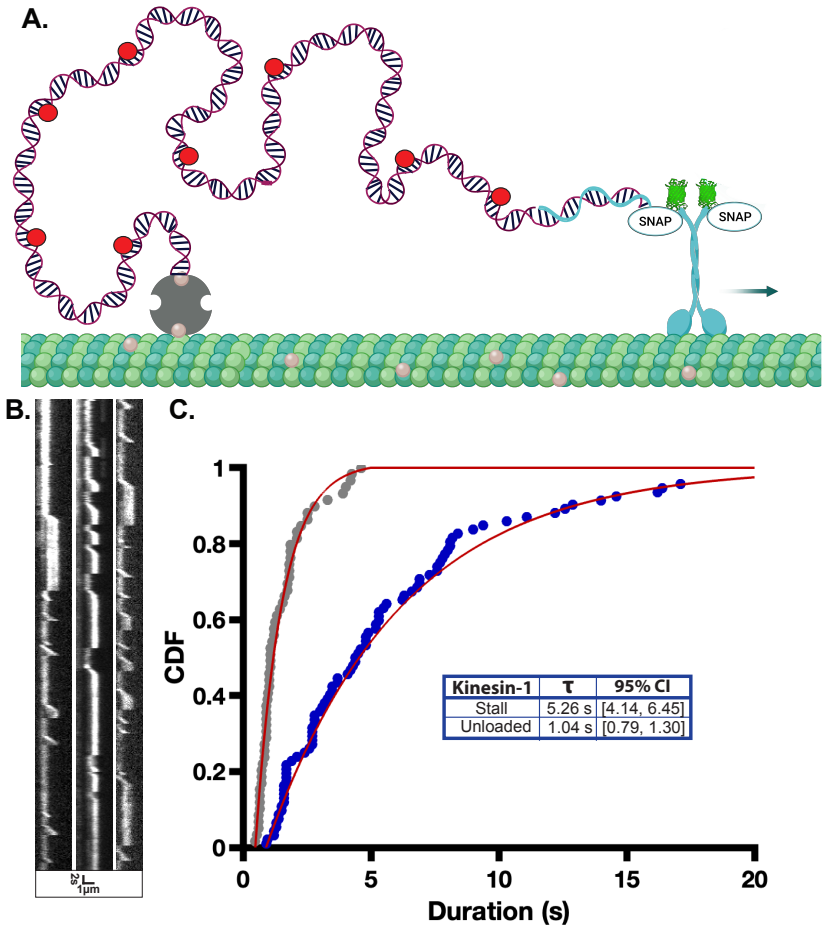

Figure. S5. Long stall durations are observed in the absence of Qdots. Because the Qdots used in our experiments are functionalized with multiple GBP nanobodies, there is the possibility that the long stall durations observed were caused by multiple motors bound to the Qdots. To test this, we ran a control experiment where, instead of labeling the motors with Qdots, we fluorescently labeled our dsDNA by incorporating 5% dCTP-Cy5 during the PCR reaction to create fluorescent dsDNA. By removing Qdots from the system, the potential for multimotor events is eliminated. (A) Diagram of control experiment. (B) TIRF kymographs of representative bright kinesin-1 DNA tensiometers collected at 5 fps, showing the typical extension and stall profiles we observed in Figure 1, with the difference that the entire dsDNA is visualized rather than the Qdot. (C) CDF plot of the fluorescent DNA tensiometer stall durations of kinesin-1, fit with a single exponential function using a maximum likelihood estimator (MEMLET). Importantly, kinesin-1 continued to have much longer stall durations than its unloaded run durations (gray points with fit; reproduced from Fig. 2A), ruling out multi-motor interactions as the cause of the long stall durations. The longer stall durations here (5.26 s) compared to the Qdot stall durations (3.01 s; Fig. 2A) is attributed to the 5 fps frame rate used in here, which makes it more difficult to detect short slip events that are observed with the 25 fps Qdot movies.

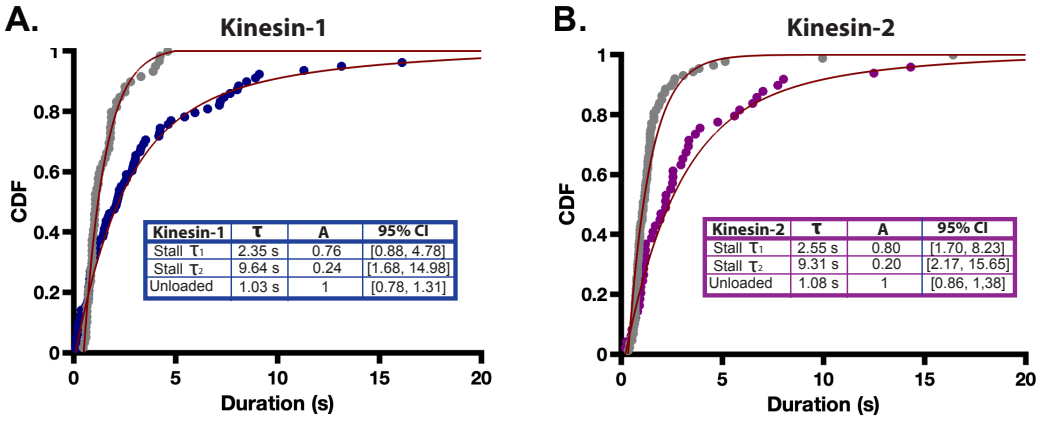

Figure. S6. Bi-exponential fits of stall durations reveal a longer duration sub-population for kinesin-1 and kinesin-2. Tensiometer stall durations of (A) kinesin-1 and (B) kinesin-2 were fit with a biexponential function using a maximum likelihood estimator, MEMLET (https://michaelswoody.github.io/MEMLET/). Unloaded run durations are shown in gray for reference. Time constants (τ), relative amplitudes (A) and 95% confidence intervals for time constants are given in the accompanying tables. The rationale for why the motors would have two time constants is not clear, but it may suggest two alternative detachment pathways. Notably, both time constants are longer than the unloaded binding duration for both motors. Kinesin-3 stall durations were well fit by a single exponential function (see Fig. 2C).

Table S3. Predicted force imposed on the motor during the ramp phase

	$v_{unloaded}$ (nm/s)	v_{ramp} (nm/s)	v_{ramp} / $v_{unloaded}$	$F_{predicted}$ (pN)*
Kinesin-1	651	572	0.88	0.72
Kinesin-2	401	324	0.81	1.14
Kinesin-3	1458	1187	0.81	1.14

*Based on linear force-velocity relationship with a 6 pN stall force

Table S4. Comparison of expected and measured fraction of ramps that reach stall.

	$\tau_{unloaded}$[a] (s)	$v_{unloaded}$[b] (nm/s)	t_{950nm}[c] (s)	Predicted stall fraction[d]	Measured stall fraction[e]	Ratio[f] (measure/predict)
Kinesin-1	1.05	651	.46	0.25	0.62	2.5
Kinesin-2	1.09	401	.37	0.11	0.14	1.3
Kinesin-3	2.76	1458	.65	0.79	0.49	0.62

[a] Unloaded run durations (Fig. 2). [b] Unloaded velocities. [c] Predicted time to reach stall (950 nm extension of dsDNA; Fig 1B) based on unloaded velocities. [d] Predicted fraction of ramps that will reach stall, calculated as: p(stall) = $e^{-\frac{t_{950nm}}{t_{unloaded}}}$. [e] Measured fraction of ramps that reach stall. [f] Ratio of expected to predicted fraction of ramps that reach stall. More kinesin-1 reach stall than predicted, suggesting off-rates during ramp are slower than unloaded. In contrast, fewer kinesin-3 ramps reach stall, suggesting that off-rates during ramp are faster than unloaded.

A.

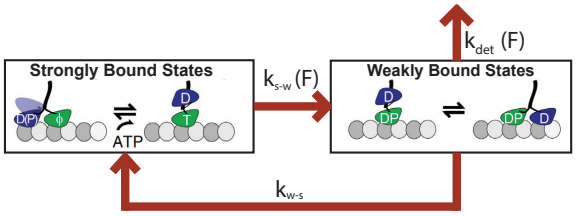

B.

Equation: $k(F) = k^0 e^{\frac{F\delta}{k_B T}}$		$k^0\ (s^{-1})$	$k_{S-W}(F)\&k_{det}(F)$ $\delta\ (nm)$
Kin1	k_{S-W}	169	-2.74
	k_{W-S}	169	-
	k_{det}	1.93	1.61
Kin2	k_{S-W}	106	-2.42
	k_{W-S}	106	-
	k_{det}	1.87	1.35
Kin3	k_{S-W}	303	-3.15
	k_{W-S}	303	-
	k_{det}	2.69	2.14

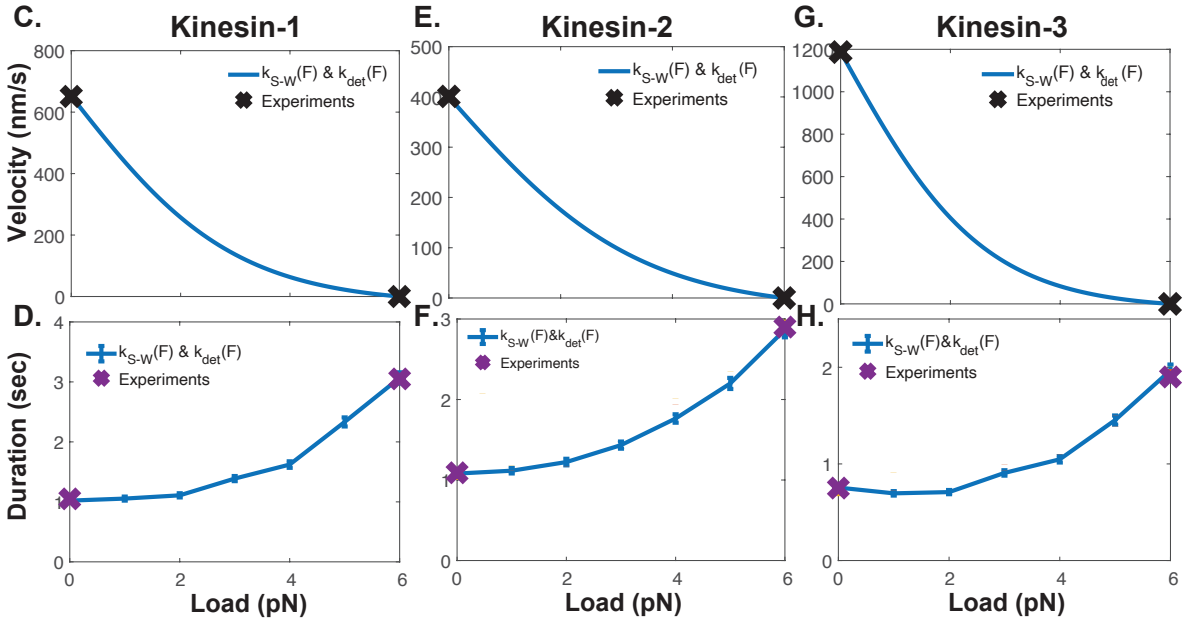

Figure. S7 Simple catch-bond model can account for all three motors. A) Diagram of $k_{S-W}(F)$ / $k_{det}(F)$ model, which is also used in Fig. 5B and C. B) Table of model parameters, where k^0 is the unloaded rate and δ is the distance parameter for each load-dependent rate constant. The two rate constants in the stepping cycle, k_{S-W} and k_{W-S} were chosen to match the unloaded velocity for each motor, and the k_{det} for each motor was chosen to match the unloaded run duration. The δ parameters for k_{S-W} were chosen such that the forward stepping rate at the 6 pN stall force was 3 s^{-1}, matching the load-independent backstepping rate. The δ parameter for k_{det} for each motor was chosen to fit the stall duration. C-H) Load dependent velocity and binding duration for kinesin-1, kinesin-2, and kinesin-3 (panel C is reproduced from Fig. 5C). Note that, based on the ramp analysis in Fig. 4 which argued that unloaded kinesin-3 runs are made up of shorter runs connected by diffusive events, we used the kinesin-3 ramp duration in panel H, rather than the unloaded run duration.

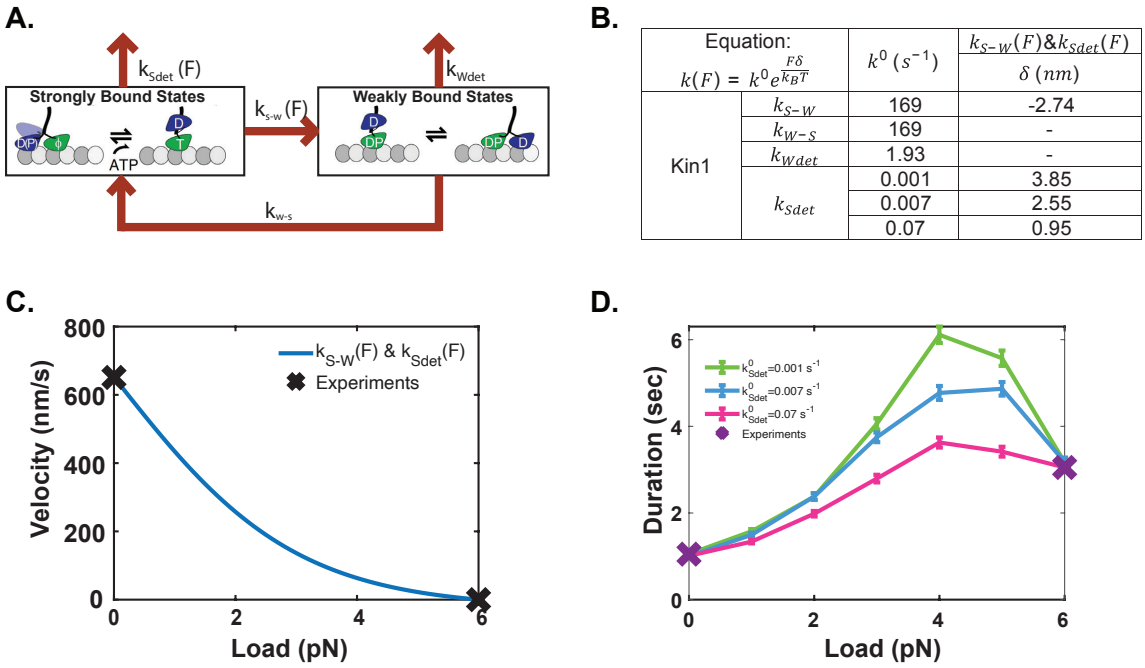

Equation: $k(F) = k^0 e^{\frac{F\delta}{k_B T}}$		$k^0\ (s^{-1})$	$k_{S-W}(F)$&$k_{Sdet}(F)$ $\delta\ (nm)$
Kin1	k_{S-W}	169	-2.74
	k_{W-S}	169	-
	k_{Wdet}	1.93	-
	k_{Sdet}	0.001	3.85
		0.007	2.55
		0.07	0.95

Figure. S8. Kinesin-1 catch-bond can also be accounted for by model incorporating load-dependent detachment from the strong-binding state. A) Diagram of $k_{S\text{-}W}$(F) / k_{Sdet}(F) model, showing the two load-dependent rate constants. B) Table of load-dependent parameters used. Unloaded k^0 for $k_{S\text{-}W}$, $k_{W\text{-}S}$, and k_{Wdet} were taken from kinesin-1 model in Fig. 5 and S7. Here, the detachment rate from the weak-binding state, k_{Wdet} (formerly called k_{det}), is load-independent, and instead k_{Sdet} is load-dependent. k_0 and δ values for k_{Sdet} were taken from estimates and measurements from Kawaguchi et al (0.001 s^{-1} and 0.007 s^{-1}) and Andreasson et al (0.07 s^{-1}) (Andreasson et al., 2015; Kawaguchi et al., 2003). In each case, the distance parameter, δ, was chosen to match the stall duration in the DNA tensiometer. As expected, slower k^0 are compensated for by larger δ. C) Force-velocity relationships are the same for all three parameter sets. D) All three models can account for the unloaded and stall durations for kinesin-1, but they each predict a different performance at intermediate loads. The reason the durations peak and fall is that at low and intermediate loads, detachment primarily occurs from the weak-binding state pathway (hence, this portion of the curve resembles the $k_{S\text{-}W}$(F) only curve in Fig. 5C), whereas at loads approaching stall, detachment occurs primarily from the strong-binding state.

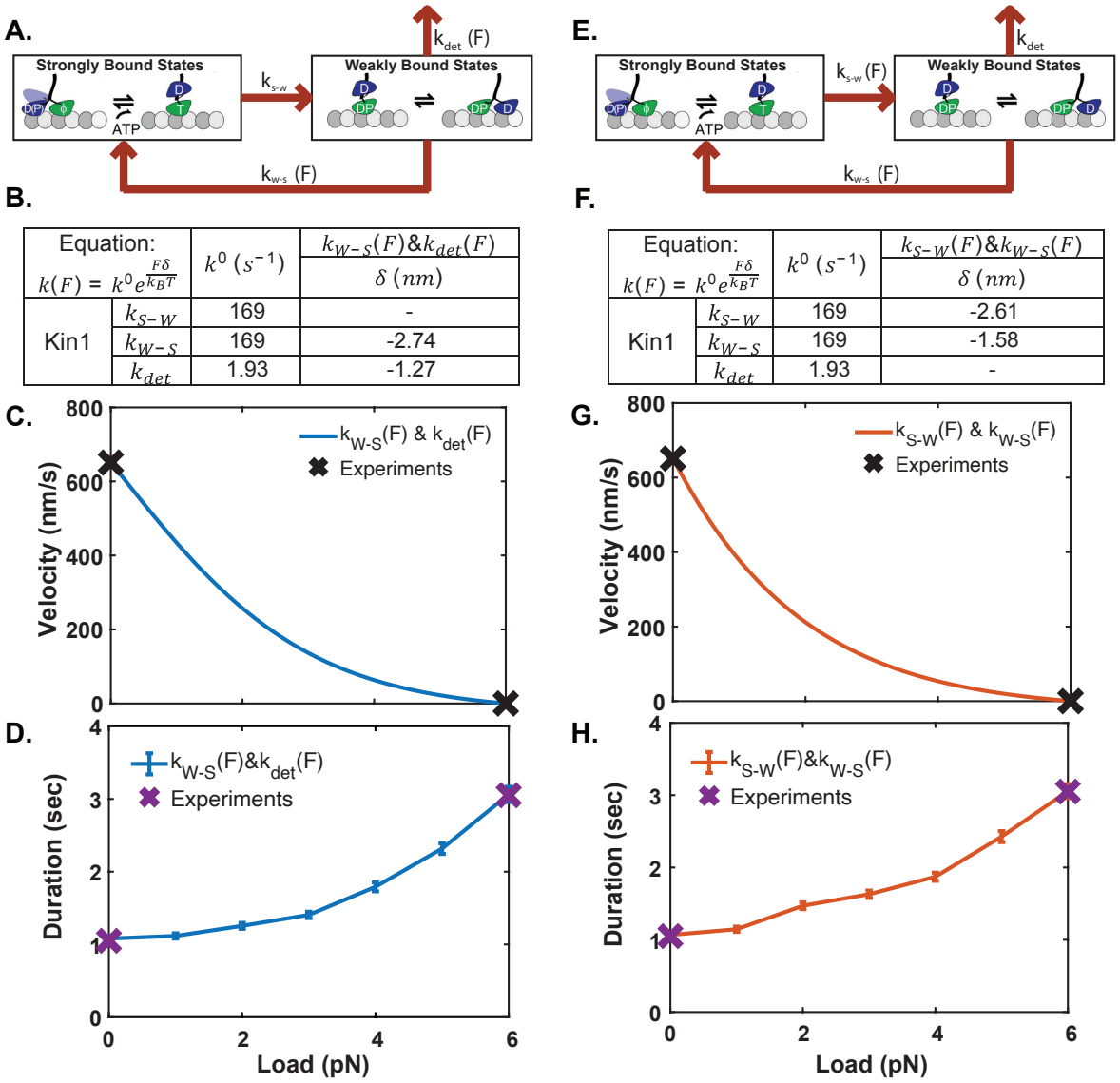

Figure. S9. Alternative models to account for catch-bond behavior. A) Diagram and B) parameters of $k_{W\text{-}S}(F)$ / $k_{det}(F)$ model. In this model, the weak-to-strong transition slows with load and the detachment rate from the weak-binding state also slows with load. In this way, detachment from the weak-binding state acts as a classic catch-bond. C and D) Load dependence of velocity and bound duration for $k_{W\text{-}S}(F)$ / $k_{det}(F)$ model. E) Diagram and F) parameters for $k_{S\text{-}W}(F)$ / $k_{W\text{-}S}(F)$ model. In this model, both transitions in the stepping cycle slow down at increasing loads, and k_{det} is load-independent. Note that $k_{S\text{-}W}$ slows with load to a greater extent than $k_{W\text{-}S}$, which results in the motor spending a greater fraction of time in the strong-binding state under load; this dynamic results in a slower motor off-rate at elevated loads. G and H) Load dependence of velocity and bound duration for $k_{S\text{-}W}(F)$ / $k_{W\text{-}S}(F)$ model.

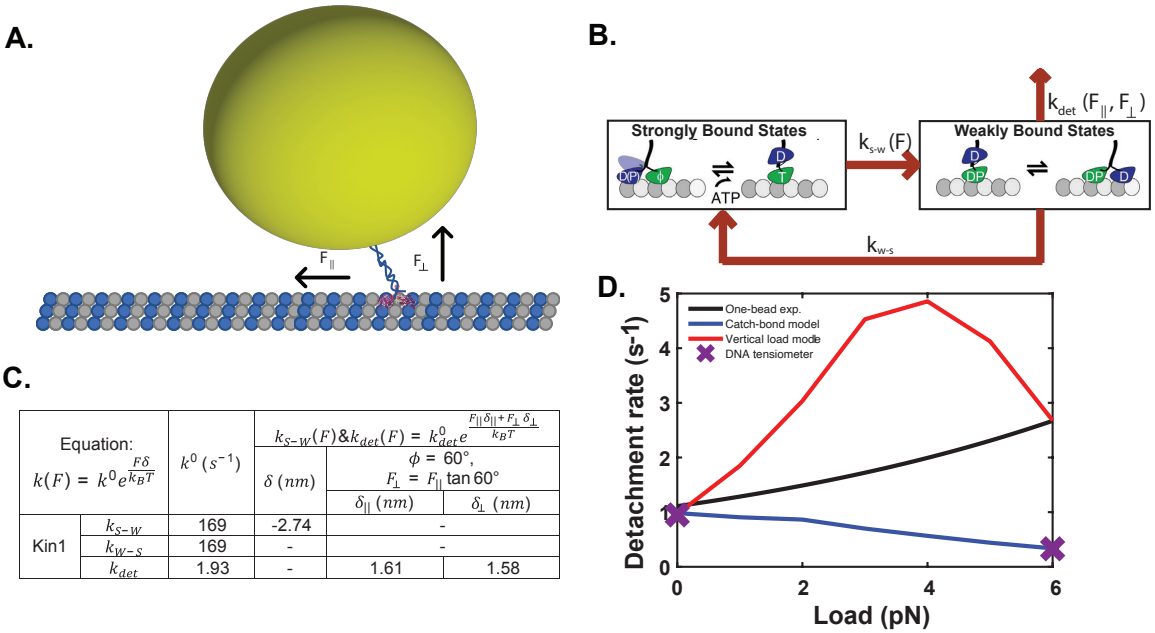

C.

Equation: $k(F) = k^0 e^{\frac{F\delta}{k_B T}}$		$k^0\ (s^{-1})$	$k_{S-W}(F)\&k_{det}(F) = k^0_{det} e^{\frac{F_\parallel \delta_\parallel + F_\perp \delta_\perp}{k_B T}}$		
			$\delta\ (nm)$	$\phi = 60°$, $F_\perp = F_\parallel \tan 60°$	
				$\delta_\parallel\ (nm)$	$\delta_\perp\ (nm)$
Kin1	k_{S-W}	169	-2.74	-	
	k_{W-S}	169	-	-	
	k_{det}	1.93	-	1.61	1.58

Figure. S10. Reconciling kinesin-1 DNA tensiometer results with published single-bead optical trapping results. A) Diagram of both perpendicular (vertical) and parallel (horizontal) forces in optical trapping studies. Note that bead (440 nm diameter) and motor (35 nm length) are not to scale. B) Diagram of model in which forces parallel to the microtubule slow $k_{S\text{-}W}$ and forces both parallel and perpendicular to the microtubule accelerate dissociation from the weak binding state, k_{det}. C) Table of parameters. Note that for k_{det}, each force component has a characteristic distance parameter, δ. These parameters have similar magnitudes, indicating that in this model, detachment has a similar sensitivity to loads oriented in the vertical versus horizontal directions. D) Comparison between simulation and experimental results for kinesin-1. Rather than duration, the detachment rate (inverse of bound duration) is plotted to enable comparison to published optical tweezer data. Purple X are DNA tensiometer results that are well fit by the model (blue line) where $F_\perp$ is zero (only forces parallel to the microtubule are involved). Note that blue detachment rate line is equivalent to bound duration from models in Fig. 5C and S7C. Black line represents experimental results from single-bead force-clamp optical tweezer results from Andreasson et al. (Andreasson et al., 2015) in which the motor angle is estimated to be 60 deg (Khataee & Howard, 2019). Equation is $k_{off}(F) = 1.11\ s^{-1} * e^{\frac{F*0.60\ nm}{4.1\ pN\ nm}}$. Red line represents model simulation results when both horizontal and vertical forces are taken into account. Note that the model captures the unloaded and stall found at the two extremities, but it overestimates the detachment rate at intermediate forces. The model dynamic that causes this overestimate is that the detachment rate rises strongly with load due to the effects of both vertical and horizontal forces, whereas the strong-to-weak transition rises more slowly with load because it is only affected by horizontal loads. Due to their exponential dependence on load, the curve peaks at intermediate loads.

SI References

Andreasson, J. O., Shastry, S., Hancock, W. O., & Block, S. M. (2015). The Mechanochemical Cycle of Mammalian Kinesin-2 KIF3A/B under Load. *Curr Biol*, *25*(9), 1166-1175. https://doi.org/10.1016/j.cub.2015.03.013

Cleary, J. M., Kim, T., Cook, A. S. I., McCormick, L. A., Hancock, W. O., & Rice, L. M. (2022). Measurements and simulations of microtubule growth imply strong longitudinal interactions and reveal a role for GDP on the elongating end. *Elife*, *11*. https://doi.org/10.7554/eLife.75931

Feng, Q., Gicking, A. M., & Hancock, W. O. (2020). Dynactin p150 promotes processive motility of DDB complexes by minimizing diffusional behavior of dynein. *Mol Biol Cell*, *31*(8), 782-792. https://doi.org/10.1091/mbc.E19-09-0495

Feng, Q., Mickolajczyk, K. J., Chen, G. Y., & Hancock, W. O. (2018). Motor Reattachment Kinetics Play a Dominant Role in Multimotor-Driven Cargo Transport. *Biophys J*, *114*(2), 400-409. https://doi.org/10.1016/j.bpj.2017.11.016

Gicking, A. M., Ma, T. C., Feng, Q., Jiang, R., Badieyan, S., Cianfrocco, M. A., & Hancock, W. O. (2022). Kinesin-1, -2, and -3 motors use family-specific mechanochemical strategies to effectively compete with dynein during bidirectional transport. *Elife*, *11*. https://doi.org/10.7554/eLife.82228

Gicking, A. M., Wang, P., Liu, C., Mickolajczyk, K. J., Guo, L., Hancock, W. O., & Qiu, W. (2019). The Orphan Kinesin PAKRP2 Achieves Processive Motility via a Noncanonical Stepping Mechanism. *Biophys J*, *116*(7), 1270-1281. https://doi.org/10.1016/j.bpj.2019.02.019

Kawaguchi, K., Uemura, S., & Ishiwata, S. (2003). Equilibrium and transition between single- and double-headed binding of kinesin as revealed by single-molecule mechanics. *Biophys J*, *84*(2 Pt 1), 1103-1113. https://doi.org/10.1016/S0006-3495(03)74926-1

Khataee, H., & Howard, J. (2019). Force Generated by Two Kinesin Motors Depends on the Load Direction and Intermolecular Coupling. *Phys Rev Lett*, *122*(18), 188101. https://doi.org/10.1103/PhysRevLett.122.188101

Kubala, M. H., Kovtun, O., Alexandrov, K., & Collins, B. M. (2010). Structural and thermodynamic analysis of the GFP:GFP-nanobody complex. *Protein Sci*, *19*(12), 2389-2401. https://doi.org/10.1002/pro.519

Rayens, N. T., Cook, K. J., McKinley, S. A., & Payne, C. K. (2022). Transport of lysosomes decreases in the perinuclear region: Insights from changepoint analysis. *Biophys J*, *121*(7), 1205-1218. https://doi.org/10.1016/j.bpj.2022.02.032

Robert, C. P. (1994). *The Bayesian Choice*. Springer.

Uppalapati M, H. Y., Shastry S, Jackson TN, Hancock WO. (2009). Methods in Bioengineering: Microfabrication and Microfluidics. In J. DZ (Ed.), (pp. 311-336).

Woody, M. S., Lewis, J. H., Greenberg, M. J., Goldman, Y. E., & Ostap, E. M. (2016). MEMLET: An Easy-to-Use Tool for Data Fitting and Model Comparison Using Maximum-Likelihood Estimation. *Biophys J*, *111*(2), 273-282. https://doi.org/10.1016/j.bpj.2016.06.019

Zaniewski, T. M., Gicking, A. M., Fricks, J., & Hancock, W. O. (2020). A kinetic dissection of the fast and superprocessive kinesin-3 KIF1A reveals a

predominant one-head-bound state during its chemomechanical cycle. *J Biol Chem*, *295*(52), 17889-17903. https://doi.org/10.1074/jbc.RA120.014961